Publ. Astron. Soc. Japan (2018) 70 (3), 48 (1–9)
doi: 10.1093/pasj/psy038
Advance Access Publication Date: 2018 April 14

Gas, dust, stars, star formation, and their evolution in M 33 at giant molecular cloud scales

Shinya Komugi,[1,2,*] Rie E. Miura,[2] Nario Kuno,[3,4] and Tomoka Tosaki[5]

[1]Department of Liberal Arts, Kogakuin University, 2665-1 Nakano-cho, Hachioji, Tokyo 192-0015, Japan
[2]Chile Observatory, National Astronomical Observatory of Japan, National Institutes of Natural Sciences, 2-21-1 Osawa, Mitaka, Tokyo 181-8588, Japan
[3]Division of Physics, Faculty of Pure and Applied Sciences, University of Tsukuba, 1-1-1 Tennodai, Tsukuba, Ibaraki 305-8571, Japan
[4]Tomonaga Center for the History of the Universe, University of Tsukuba, 1-1-1 Tennodai, Tsukuba, Ibaraki 305-8571, Japan
[5]Joetsu University of Education, Yamayashiki-machi, Joetsu, Niigata 943-8512, Japan

*E-mail: skomugi@cc.kogakuin.ac.jp

Received 2017 November 29; Accepted 2018 March 13

Abstract

We report on a multi-parameter analysis of giant molecular clouds (GMCs) in the nearby spiral galaxy M 33. A catalog of GMCs identifed in ^{12}CO(J = 3–2) was used to compile associated ^{12}CO(J = 1–0), dust, stellar mass, and star formation rate. Each of the 58 GMCs are categorized by their evolutionary stage. Applying the principal component analysis on these parameters, we construct two principal components, PC1 and PC2, which retain 75% of the information from the original data set. PC1 is interpreted as expressing the total interstellar matter content, and PC2 as the total activity of star formation. Young ($<$ 10 Myr) GMCs occupy a distinct region in the PC1–PC2 plane, with lower interstellar medium (ISM) content and star formation activity compared to intermediate-age and older clouds. Comparison of average cloud properties in different evolutionary stages imply that GMCs may be heated or grow denser and more massive via aggregation of diffuse material in their first $\sim$ 10 Myr. The PCA also objectively identified a set of tight relations between ISM and star formation. The ratio of the two CO lines is nearly constant, but weakly modulated by massive star formation. Dust is more strongly correlated with the star formation rate than the CO lines, supporting recent findings that dust may trace molecular gas better than CO. Stellar mass contributes weakly to the star formation rate, reminiscent of an extended form of the Schmidt–Kennicutt relation with the molecular gas term substituted by dust.

Key words: galaxies: ISM — galaxies: star formation — galaxies: statistics — ISM: clouds

1 Introduction

The transition from gas to stars is a complex process involving various spatial and temporal scales. Observationally, much of the star formation take place within giant molecular clouds (GMCs) which are typically a few $\times$ 10 to $\sim$ 100 pc in size. However, current knowledge of the general law of star formation is limited to semi-global scales over kiloparsecs, where the relation between molecular gas and star formation is characterized by a simple power law, the

© The Author(s) 2018. Published by Oxford University Press on behalf of the Astronomical Society of Japan. This is an Open Access article distributed under the terms of the Creative Commons Attribution License (http://creativecommons.org/licenses/by/4.0/), which permits unrestricted reuse, distribution, and reproduction in any medium, provided the original work is properly cited.

Downloaded from https://academic.oup.com/pasj/article-abstract/70/3/48/4970741 by Library of Chinese Academy of Sciences user on 02 August 2019

Schmidt–Kennicutt (SK) relation (Kennicutt 1998; Komugi et al. 2005 and references therein).

The SK relation is known to break down at the scale of individual GMCs (Onodera et al. 2010) when using diffuse molecular gas tracers like the ^{12}CO($J = 1$–0) emission. This has been attributed to the different evolutionary stage of GMCs (e.g., Kawamura et al. 2009) which become evident at the $\sim$100-parsec scale (Onodera et al. 2010). Komugi et al. (2012) support this by showing that the dispersion of the SK relation becomes small when star-forming regions at the same age are used. When using denser and/or warmer gas, such as that traced by the ^{12}CO($J = 3$–2) line, the relation is generally tighter (Komugi et al. 2007; Muraoka et al. 2007, 2016; Iono et al. 2009) and this has been explained by the higher CO transition tracing molecular gas that is spatially and temporally closer to the actual site of star formation (c.f., Wu et al. 2005 using HCN emission). Onodera et al. (2012) reveal a connection between the two CO tracers and star formation, finding that larger GMCs tend to have higher ^{12}CO($J = 3$–2)/^{12}CO($J = 1$–0) ratios (r_{31}), along with a higher star formation rate (*SFR*).

The connection of dust and star formation is also important, as dust grain surfaces act as a catalysis for molecular gas production. Recent studies (Wolfire et al. 2010; Paradis et al. 2012; Scoville et al. 2016) also indicate that dust may trace molecular gas better than CO in some regions where gas is not dense enough to shield itself against UV photon dissociation (Hollenbach & Tielens 1999). Stellar mass may be another parameter which controls star formation at various scales. Shi et al. (2011) and Rahmani, Lianou, and Barmby (2016) show that when the SK relation is extended to include the stellar mass, the dispersion becomes smaller both globally and within galaxies at kiloparsec scales. Stellar contribution is also theoretically expected from stability analysis (Dib et al. 2017) and pressure-regulated star formation (Blitz & Rosolowsky 2006 and others).

It is becoming increasingly clear that, at the scale of GMCs, star formation is not explained by a single parameter equation such as the SK relation; it is better described as a time-evolving equilibrium state between the interstellar medium (ISM) and star formation. In this paper, we attempt to formalize this state using a multi-parameter analysis on a sample of GMCs in the nearby spiral galaxy M 33.

2 Data

The Nobeyama Radio Observatory (NRO) M 33 All-Disk Survey of Giant Molecular Clouds (MAGiC) (Kuno et al. 2011) observed the optical disk ($30' \times 30'$, corresponding to 7.3 kpc $\times$ 7.3 kpc) in the nearby spiral galaxy M 33 using the ^{12}CO($J = 1$–0) line at $19''$ resolution, corresponding to 80 pc (Tosaki et al. 2011). A corresponding map was obtained at ASTE telescope (Ezawa et al. 2004; Kohno 2005) in ^{12}CO($J = 3$–2) at $25''$ (100 pc) resolution by Miura et al. (2012), and in the 1.1-mm continuum by Komugi et al. (2011a) at $40''$ (160 pc) resolution. In this paper, we use ^{12}CO($J = 3$–2), ^{12}CO($J = 1$–0) and *SFR* derived from combinations of Hα and 24 μm, for 71 GMCs catalogued by Miura et al. (2012). In order to circumvent the uncertainties associated with the CO to H_2 conversion factor, throughout this paper we use CO luminosities L'_{3-2} and L'_{1-0} instead of converting them to molecular gas masses.

The catalog by Miura et al. (2012) also includes a measure of the evolutionary stage of the GMCs, Types A through D, based on stellar group identifications using the Massey et al. (2006) star catalog and Padova stellar synthesis tracks (Marigo et al. 2008; Girardi et al. 2010). In this paper, we use only Type B, C, and D GMCs, because only one Type A GMC was identified in the catalog, and further it was not detected at 1.1 mm. Type B are young GMCs which are associated with relatively small H II regions but not with young stellar groups (YSGs), and are at a stage approximately 3–7 Myr after the first formation of massive OB stars. Type C GMCs are associated with both H II regions and YSGs less than 10 Myr old, indicating that they are 10–20 Myr in age. Type D GMCs have H II regions and relatively old (10–30 Myr) stellar groups, and are 20–40 Myr in age (see Miura et al. 2012).

We identified cold dust clumps associated with each of these catalogued GMCs using the 1.1-mm continuum map from Komugi et al. (2011a). A box of $54''$ on the side, which is two times the detector FWHM of the observation, was centered on the H II region to search for a 1.1-mm peak. The angular size of the 1.1-mm beam covers the entire GMC, so its peak value can be used to obtain the total dust mass M_d. We assume a dust emissivity of $\kappa = 0.114\ \mathrm{m^2\ kg^{-1}}$, and corrected for the dust temperature using the color temperature between 1.1-mm and Spitzer MIPS 160 μm flux. Details of the 1.1-mm data and temperature derivation are found in Komugi et al. (2011a).

The stellar mass M_* of the corresponding regions were derived from a K_S (2.1 μm) image from the 2MASS Large Galaxy Survey (Jarrett et al. 2003). The image was background subtracted using planar interpolation from regions well away from the galaxy, and then convolved to $40''$ resolution to match the 1.1-mm image. A Galactic extinction correction of 0.022 mag was applied, based on the NASA Extragalactic Database (NED). The K_S brightness was then converted to stellar mass using relations in Blitz and Rosolowsky (2006), assuming galactic inclination of 55° (de Vaucouleurs 1959).

Downloaded from https://academic.oup.com/pasj/article-abstract/70/3/48/4970741 by Library of Chinese Academy of Sciences user on 02 August 2019

Table 1. Variance of principle components for luminosity.*

Values	PC_1	PC_2	PC_3	PC_4	PC_5
Eigenvalue (variance)	2.68 ± 0.14	1.23 ± 0.02	0.81 ± 0.01	0.42 ± 0.00	0.07 ± 0.00
Proportion of variance	0.52 ± 0.01	0.24 ± 0.01	0.16 ± 0.00	0.08 ± 0.00	0.01 ± 0.00
Cumulative proportion	0.52	0.75	0.91	0.99	1.00

*The eigenvalues of each of the PCs correspond to the amount of information that is projected on to the PC. The propertion of variance is its ratio to the total amount of information, i.e., the variance divided by $n = 5$.

Table 2. Variance of principle components for surface density.*

Values	PC_1	PC_2	PC_3	PC_4	PC_5
Eigenvalue (variance)	2.64 ± 0.13	1.30 ± 0.03	0.91 ± 0.02	0.29 ± 0.00	0.07 ± 0.00
Proportion of variance	0.51 ± 0.01	0.25 ± 0.01	0.17 ± 0.01	0.06 ± 0.00	0.01 ± 0.00
Cumulative proportion	0.50	0.76	0.93	0.99	1.00

*Same as table 1, but for surface densities.

Peaks identified in 1.1-mm and K_S were both inspected by eye to ensure that they are discrete clumps and are associated with the H II region and GMCs identified in both CO lines. Out of the 71 regions catalogued in Miura et al. (2012), 58 GMCs were identified in all of the two CO lines, M_d, *SFR*, and M_*. The final sample consists of 10 Type B, 30 Type C, and 18 Type D GMCs. All following analyses in this paper use this final sample.

3 Principal component analysis

We utilize the principal component analysis (PCA) approach to the catalogue of GMCs. The PCA works on an arbitrary n number of parameters x, and constructs n new axes (principal components; PCs) using a linear combination of these n parameters, so that the new axes "better describe" the characteristics of the sample than the original parameters. Formally,

$$PC_i = \alpha_{i,1}x_1 + \alpha_{i,2}x_2 + ... + \alpha_{i,n}x_n, \quad (1)$$

where x_i terms are the explanatory parameters of the GMC samples, which are $\log SFR$, $\log L'_{3-2}$, $\log L'_{1-0}$, $\log M_*$, and $\log M_d$. Since the parameters x_i have different dynamical range and units, they are normalized so that their average is zero and variance is unity. The coefficients α are normalized so that

$$\sqrt{\alpha_{i,1}^2 + \alpha_{i,2}^2 + ... + \alpha_{i,n}^2} = 1. \quad (2)$$

The amount of information that is projected on to the new PC can be measured by their variance (eigenvalue). In the present study, $n = 5$, and the total variance of 5 is conserved after the projection of the axes. The coefficient α represents the amount of contribution that each parameter x_i has on PC_i. The first principal component, PC_1, is defined so that the variance of data around this axis is maximized. PC_2 is then defined orthogonal to PC_1, having the next largest variance, and so on. The nth principle component PC_n will have the minimum variance. In short, PC_1 is a parameter which best describes the GMC sample, and PC_2 follows.

Although molecular clouds are characterized by their CO luminosities and their associated dust, stellar mass, and *SFR*, the SK relation is usually described in terms of surface densities of each quantity. We have applied the PCA in two ways, to both luminosity (mass) and surface densities. The surface density of each parameter was calculated by dividing each quantity by the projected area of the molecular cloud as derived in Miura et al. (2012), and the stellar surface density was derived directly from the K_S brightness.

4 Results

Tables 1 and 2 summarize the variances determined for the PCs. For both cases, PC_1, PC_2, and PC_3 have variances adding up to more than 90% of the total information in the original data set. For PC_4 and PC_5, the amount of information is significantly reduced from the original axes; the variances around these PCs decrease from 1 to 0.42 (0.29) and 0.07 (0.07), corresponding to only 8%(6%) and 1%(1%) of the total variance, respectively, where values in parentheses are for surface densities. Tables 3 and 4 summarize the coefficients α. The PCA is a purely mathematical operation, so a physical interpretation must be given to the new PCs. For a robust interpretation, we adopt only the terms that contribute significantly to the new PCs, and ignore terms with coefficients smaller than 0.45 [corresponding to

Downloaded from https://academic.oup.com/pasj/article-abstract/70/3/48/4970741 by Library of Chinese Academy of Sciences user on 02 August 2019

Table 3. PCA coefficients α for luminosities.*

Original parameters	PC_1	PC_2	PC_3	PC_4	PC_5
$\log L'_{1-0}$	**0.50 ± 0.02**	**−0.49 ± 0.02**	−0.26 ± 0.01	0.06 ± 0.00	**−0.67 ± 0.00**
$\log L'_{3-2}$	**0.56 ± 0.01**	−0.34 ± 0.02	−0.10 ± 0.01	0.21 ± 0.01	**0.72 ± 0.00**
$\log M_{\rm d}$	**0.49 ± 0.01**	0.23 ± 0.03	0.32 ± 0.02	**−0.78 ± 0.00**	0.00 ± 0.00
$\log M*$	0.21 ± 0.03	**0.60 ± 0.02**	**−0.77 ± 0.02**	0.00 ± 0.02	0.01 ± 0.00
$\log SFR$	0.40 ± 0.02	**0.48 ± 0.02**	**0.48 ± 0.02**	**0.59 ± 0.00**	−0.19 ± 0.00

*Coefficients which contribute significantly to the PCs are shown in bold.

Table 4. PCA coefficients α for surface densities.*

Original parameters	PC_1	PC_2	PC_3	PC_4	PC_5
$\log L'_{1-0}$	**0.49 ± 0.02**	**−0.45 ± 0.01**	−0.35 ± 0.02	−0.02 ± 0.00	**−0.66 ± 0.00**
$\log L'_{3-2}$	**0.57 ± 0.01**	−0.28 ± 0.02	−0.24 ± 0.01	0.08 ± 0.01	**0.73 ± 0.00**
$\log M_{\rm d}$	**0.48 ± 0.02**	0.24 ± 0.03	**0.51 ± 0.02**	**−0.68 ± 0.00**	0.05 ± 0.00
$\log M*$	0.07 ± 0.03	**0.65 ± 0.03**	**−0.71 ± 0.03**	−0.26 ± 0.01	0.01 ± 0.01
$\log SFR$	0.44 ± 0.02	**0.49 ± 0.03**	0.25 ± 0.03	**0.69 ± 0.01**	−0.16 ± 0.00

*Coefficients which contribute significantly to the PCs are shown in bold.

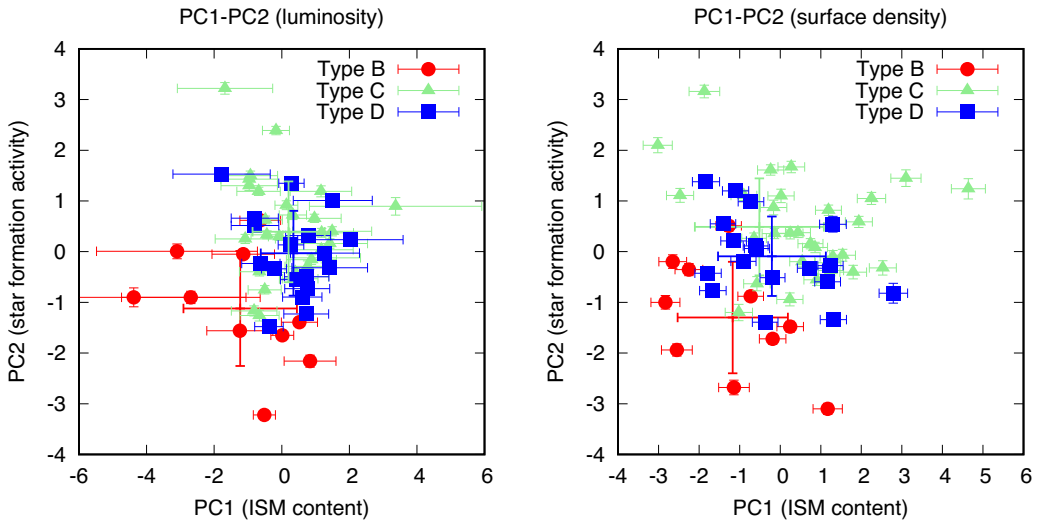


Fig. 1. Total ISM content (PC1) and star formation activity (PC2) in M 33, when considering luminosities (left) and surface densities (right). For both panels, red circles indicate young Type B GMCs, green triangles indicate intermediate Type C GMCs, and blue squares indicate old Type D GMCs (see section 2 for their corresponding ages). The crosses indicate the average and standard deviation for each GMC group. (Color online)

$\alpha^2 = 1/n$ in equation (2) for $n = 5$]. Coefficients which contribute significantly to the PCs are similar for luminosities and surface densities, except for the case of PC3. They are shown in bold in tables 3 and 4.

4.1 Robustness of PCA analysis

The PCA analysis is sensitive to uncertainties in the original data set. Therefore, we estimate the uncertainty in the variances, PCA scores, and coefficients by using a bootstrapping method. We create a resampled data set where values for each original parameter for each GMC follow a Gaussian distribution, with 30% standard deviation with respect to the original data. The assumed uncertainty of 30% corresponds to the typical error in the L'_{3-2} measurement, which has the largest observational error in the data sets, and therefore gives a conservative estimate of how the PCA analysis can be affected by intrinsic uncertainties in the data set. We create 10^4 such resampled data sets, and run the PCA analysis on each of them. The error estimates in figure 1 and tables 1 through 4 correspond to the standard deviation of each value computed from bootstrapping. The errors for the variances, coefficients, and PCA scores show that the PCA analyses are stable and results

Downloaded from https://academic.oup.com/pasj/article-abstract/70/3/48/4970741 by Library of Chinese Academy of Sciences user on 02 August 2019

presented here are not severely affected by observational uncertainties.

4.2 PC_1 and PC_2

The first two PCs contain the most information in the data set. PC_1 has the largest variance, contributing $\sim 50\%$ to the total value, thus best characterizing the star-forming GMCs. From tables 3 and 4, PC_1 is contributed almost equally by L'_{1-0}, L'_{3-2}, and $M_{\rm d}$, which all express quantities of the ISM, all with positive coefficients. PC_1 may be interpreted as a scaling factor indicating the *total ISM content* of the regions. PC_2 correlates positively with *SFR* and stellar mass, both of which are related to star formation in the ISM. A higher *SFR*, and its integration over time (the stellar mass) lead to a higher PC_2. It is also anti-correlated with L'_{1-0}, which indicates that PC_2 increases for a higher *SFR per molecular gas mass*, i.e., the efficiency of star formation. PC_2 may be interpreted as a measure of the *star formation activity*, both instantaneous and over a longer timescale. The first two PCs combined account for $\sim 75\%$ of the total information. They can be written as

$$\begin{aligned} {\rm PC}'_1 =& 0.50 \pm 0.02\ (0.49 \pm 0.02) \log \tilde{L}'_{1-0} \\ &+ 0.56 \pm 0.01\ (0.57 \pm 0.01) \log \tilde{L}'_{3-2} \\ &+ 0.49 \pm 0.01\ (0.48 \pm 0.02) \log \tilde{M}_{\rm d}, \end{aligned} \tag{3}$$

$$\begin{aligned} {\rm PC}'_2 =& 0.60 \pm 0.02\ (0.65 \pm 0.03) \log \tilde{M}_* \\ &+ 0.48 \pm 0.02\ (0.49 \pm 0.03) \log \tilde{SFR} \\ &- 0.49 \pm 0.02\ (-0.45 \pm 0.01) \log \tilde{L}'_{1-0}, \end{aligned} \tag{4}$$

where the prime symbols on the left-hand side indicate that insignificant terms on the right-hand side have been omitted, and the tilde symbols on the right-hand side indicate that the (logarithm of the) values are normalized, as explained in section 3. Values in parentheses indicate the case for surface densities (same hereafter). Figure 1 shows PC_1 versus PC_2, categorized by their evolutionary stages. For both luminosity and surface density, young Type B molecular clouds are distributed in a different region from intermediate (Type C) and older (Type D) clouds, such that they have less ISM content and star formation activity.

4.3 PC_3

The third PC has a variance that is lower than unity. This indicates that the amount of information has decreased from the original axes, i.e., that PC_3 does not explain the properties of molecular clouds better than the original parameters. It is dominated by contribution from the stellar mass, with smaller contribution from SFR in the case of luminosities, and dust in the case of surface densities. The physical interpretation of PC_3 is unclear, as the contributing parameters are different between luminosities and surface densities. Here we will not attempt to give PC_3 a physical interpretation.

4.4 PC_4 and PC_5

The last two PCs have the least variance in the given data sets, and can be used to detect relations between variables. Since the PC scores of individual clouds average to zero, we can write

$$\begin{aligned} {\rm PC}'_4 =& 0.59 \pm 0.00\ (0.69 \pm 0.01) \log \tilde{SFR} \\ &- 0.78 \pm 0.00\ (-0.68 \pm 0.00) \log \tilde{M}_{\rm d} = 0, \end{aligned} \tag{5}$$

$$\begin{aligned} {\rm PC}'_5 =& 0.72 \pm 0.00\ (0.73 \pm 0.00) \log \tilde{L}'_{3-2} \\ &- 0.67 \pm 0.00\ (-0.66 \pm 0.00) \log \tilde{L}'_{1-0} = 0. \end{aligned} \tag{6}$$

Equations (5) and (6) indicate that there are two independent correlations in this data set, one between $\log M_{\rm d}$ and $\log SFR$, and another between $\log L'_{3-2}$ and $\log L'_{1-0}$. The relation between the original parameters can be derived by converting equations (5) and (6) to "untilded" values using the average and standard deviation of each parameter. These averages and deviations are given in table 5. Alternatively, a simple least-squares fitting to the original parameters (in which case the PCA is used only for a selection of important parameters) can be used for comparison with the literature. The two procedures give

$$\begin{aligned} &\log SFR = 3.4 \log M_{\rm d} - 12.5 \quad ({\rm PC}'_4 = 0) \\ &\log SFR = (1.4 \pm 0.3) \log M_{\rm d} - (7.1 \pm 0.8) \\ &\qquad\qquad ({\rm least\text{-}squares\ fitting}) \end{aligned} \tag{7}$$

and

$$\begin{aligned} &\log L'_{3-2} = 0.95 \log L'_{1-0} + 0.65 \quad ({\rm PC}'_5 = 0) \\ &\log L'_{3-2} = (0.97 \pm 0.06) \log L'_{1-0} + 0.7 \pm 0.3 \\ &\qquad\qquad ({\rm least\text{-}\ squares\ fitting}) \end{aligned} \tag{8}$$

for luminosity, and

$$\begin{aligned} &\log \Sigma_{SFR} = 3.1 \log \Sigma_{\rm d} - 2.1 \quad ({\rm PC}'_4 = 0) \\ &\log \Sigma_{SFR} = (2.1 \pm 0.3) \log \Sigma_{\rm d} - (5.1 \pm 0.3) \\ &\qquad\qquad ({\rm least\text{-}squares\ fitting}) \end{aligned} \tag{9}$$

Downloaded from https://academic.oup.com/pasj/article-abstract/70/3/48/4970741 by Library of Chinese Academy of Sciences user on 02 August 2019

Table 5. Average physical parameters of the sample GMCs.

Parameters	Units	Type B	Type C	Type D	All
$\log L'_{1-0}$	K km s^{-1} pc^2	4.10 ± 0.41	4.14 ± 0.26	4.22 ± 0.27	4.16 ± 0.29
$\log L'_{3-2}$	K km s^{-1} pc^2	4.56 ± 0.42	4.77 ± 0.29	4.83 ± 0.26	4.75 ± 0.31
$\log M_{\rm d}$	$M_\odot$	2.52 ± 0.33	2.74 ± 0.24	2.78 ± 0.21	2.72 ± 0.26
$\log M_*$	$M_\odot$	4.89 ± 0.31	5.51 ± 0.32	5.40 ± 0.46	5.37 ± 0.43
$\log SFR$	$M_\odot$ yr^{-1}	− 4.03 ± 0.64	− 3.03 ± 0.61	− 3.18 ± 0.46	− 3.25 ± 0.67
$\log \Sigma_{L'1-0}$	K km s^{-1}	0.59 ± 0.35	0.63 ± 0.30	0.57 ± 0.24	0.61 ± 0.29
$\log \Sigma_{L'3-2}$	K km s^{-1}	1.05 ± 0.30	1.26 ± 0.33	1.18 ± 0.28	1.20 ± 0.32
$\log \Sigma_{\rm d}$	$M_\odot$ pc^{-2}	− 0.99 ± 0.19	− 0.76 ± 0.22	− 0.87 ± 0.18	− 0.83 ± 0.22
$\log \Sigma_*$	$M_\odot$ pc^{-2}	1.38 ± 0.40	2.00 ± 0.31	1.75 ± 0.26	1.82 ± 0.39
$\log \Sigma_{SFR}$	$M_\odot$ yr^{-1} pc^{-2}	− 7.54 ± 0.51	− 6.53 ± 0.62	− 6.83 ± 0.60	− 6.80 ± 0.69
Cloud radius	pc	33 ± 10	33 ± 7	39 ± 10	

and

$$\log \Sigma_{L'(3-2)} = 1.00 \log \Sigma_{L'(1-0)} + 0.59 \quad (\mathrm{PC}'_5 = 0)$$
$$\log \Sigma_{L'(3-2)} = (0.99 \pm 0.06) \log \Sigma_{L'(1-0)} + (0.60 \pm 0.04) \quad \text{(least-squares fitting)} \tag{10}$$

for surface density. Equations (7) through (10) indicate that a classical SK relation is not found between individual molecular clouds, but instead expose the correlation between *SFR* and dust. Figure 2 shows equations (7) and (9) along with an SK relation plot comparing the *SFR* with dust and the two CO lines.

5 Discussion

5.1 Molecular gas and star formation at GMC scales

A correlation between molecular gas and *SFR* is nonexistent when molecular gas is traced by the ^{12}CO(J = 1–0) line [right-hand panels of figure 2 with correlation coefficient 0.18 (top) and 0.20 (bottom)] but slightly more correlated when using higher density tracers like the ^{12}CO(J = 3–2) line [middle panels of figure 2 with correlation coefficient 0.40 (top) and 0.42 (bottom)]. This is consistent with previous studies which find that molecular lines which trace denser or warmer molecular gas is more strongly correlated with star formation (Komugi et al. 2007; Muraoka et al. 2007, 2016; Iono et al. 2009), presumably because they trace gas that is spatially and temporally closer to star-forming molecular gas. The correlation between *SFR* and dust mass is much more pronounced [equations (7) and (9), left-hand panels of figure 2 with correlation coefficient 0.64 (top) and 0.66 (bottom)] than the relation for CO. If we assume that molecular gas is a direct precursor of star formation, and that their quantities are intrinsically correlated, the strong dust–*SFR* correlation supports recent studies which claim that dust emission traces molecular gas better than CO (Wolfire et al. 2010; Paradis et al. 2012; Scoville et al. 2016). The basis behind this may be the existence of "CO-dark" molecular gas, in the diffuse outskirts of the molecular clouds where CO can be dissociated by UV photons but hydrogen molecules survive due to self-shielding (Hollenbach & Tielens 1999; Wolfire et al. 2010). In this case, the strong correlation between *SFR* and dust may be specific to M 33 because of its relatively low metallicity [12 + log (O/H) = 8.48 in the central region; Bresolin 2011, since the amount of CO-dark gas is inferred to increase in low-metallicity systems (Israel 1997; Leroy et al. 2007; Komugi et al. 2011b). Alternatively, a strong correlation between dust and *SFR* could imply that the 1.1-mm observation is predominantly tracing dense gas that is linked directly to star formation, since millimeter dust is optically thin where CO would be optically thick and unable to accurately trace the gas quantity.

5.2 GMC evolution

The distribution of GMCs in figure 1 has implications for how GMCs evolve after stars form. Directly after the onset of star formation represented by Type B clouds, both the total ISM content (PC_1) and SF activity (PC_2) increase significantly, both in luminosity and surface density. This is a natural consequence of all parameters contributing to PC_1 and PC_2 increasing from Type B to Type C/D (see table 5). Although the increases of each parameter contributing to PC_1 and PC_2 are insignificant or small considering their standard deviations, the PCs with these parameters combined result in a distinct distribution of ISM content (PC_1) and SF activity (PC_2) between Type B and Type C/D.

Nominally, an increase in $\log L'_{3-2}$ can be attained either from collapse (increase in density) or heating of diffuse gas traced in ^{12}CO(J = 1–0). r_{31} indeed increases significantly from Type B to C (Miura et al. 2012). The increase in r_{31} could be due to gas heating by the increased star formation event, or alternatively, could indicate that ISM is

Downloaded from https://academic.oup.com/pasj/article-abstract/70/3/48/4970741 by Library of Chinese Academy of Sciences user on 02 August 2019

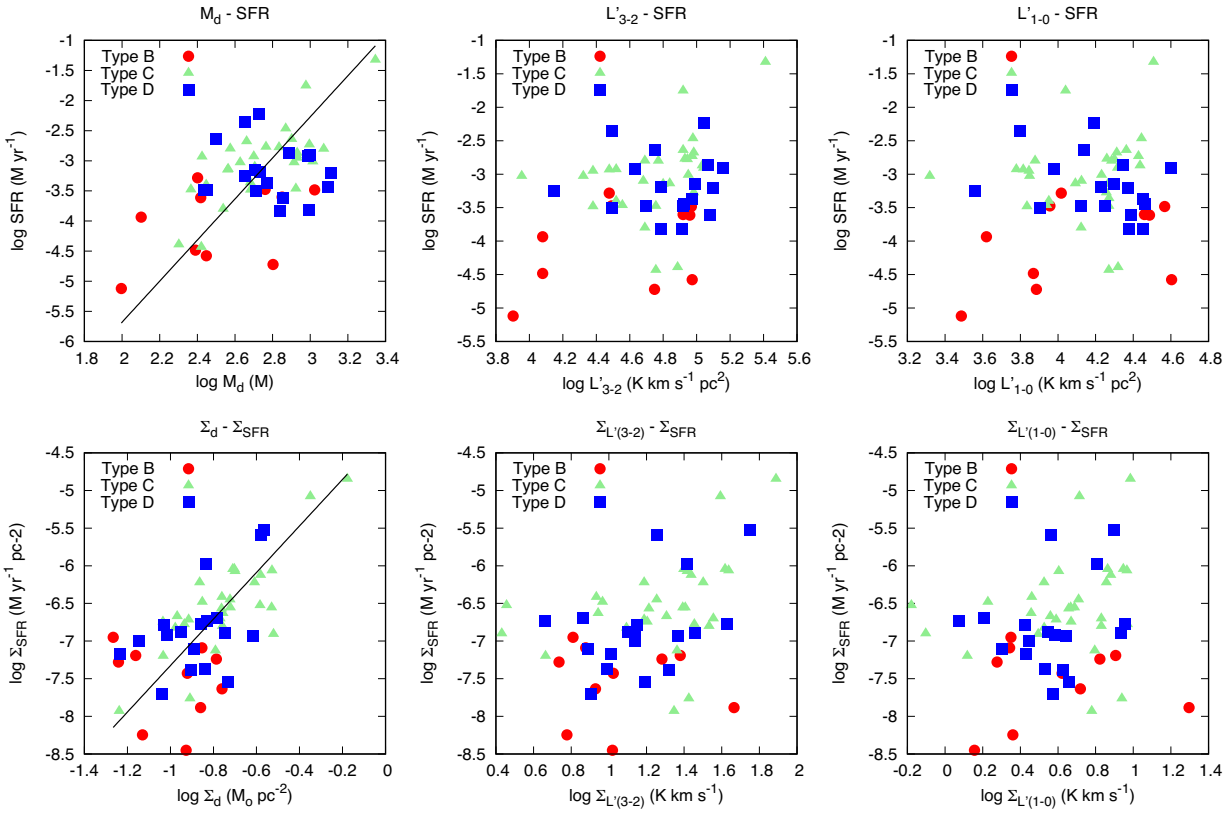


Fig. 2. *SFR* as a function of dust (left), ^{12}CO($J = 3$–2) (middle), and ^{12}CO($J = 1$–0) (right). Top panels are for values in luminosity, bottom for surface densities. Symbols are coded as in figure 1. The black lines in the left-hand panels indicate equations (7) and (9), obtained by setting $PC'_4 = 0$. (Color online)

being aggregated from the diffuse material. ISM build-up may explain the 60% increase in dust mass from Type B to C, although a part of the increased dust mass may be due to enrichment by red supergiants and/or the death of massive stars occurring during the $\sim$10-Myr lifetime of Type B clouds (Dunne et al. 2003; Hernández et al. 2006; Eldridge & Relaño 2011).

Clouds with larger mass tend to have higher r_{31}, higher *SFR*, and increased star formation efficiency (Onodera et al. 2012; Miura et al. 2014), resulting in higher PC_1 and PC_2. Figure 1 (right) shows that the density of ISM content and SF activity increase as well. This is because the average size of the clouds determined from ^{12}CO($J = 3$–2), given in table 5 [taken from table 6 in Miura et al. (2012)], indicate no size difference between Type B and C clouds. A slight increase in cloud size for Type D may explain the slight surface density decrease in PC_1 and PC_2 from Type C to D.

5.3 Dynamical equilibrium of the interstellar and stellar phases

Although parameters which contribute weakly (i.e., with coefficients smaller than 0.45 in tables 3 and 4) are dropped from the analyses above, it is worth noting some relations with these weakly contributing parameters for comparison with previous studies. From tables 3 and 4, it can be seen that PC_5 is almost completely dominated by contributions from L'_{3-2} and L'_{1-0}. However, the effect of log *SFR* is visible when the three parameters are seen in three-dimensional space, where the two CO luminosities and the *SFR* comprise a plane expressed by

$$\log L'_{3-2} = 1.0 \log L'_{1-0} + 0.12 \log SFR + 2.3 \quad (PC'_5 = 0), \tag{11}$$

$$\begin{aligned} \log L'_{3-2} = {} & (0.93 \pm 0.05) \log L'_{1-0} \\ & + (0.12 \pm 0.02) \log SFR \\ & + 1.3 \pm 0.2 \quad \text{(least-squares fitting)} \end{aligned} \tag{12}$$

for luminosities, and

$$\log \Sigma_{L'3-2} = 1.0 \log \Sigma_{L'1-0} - 0.10 \log \Sigma_{SFR} + 2.9 \quad (PC'_5 = 0), \tag{13}$$

$$\begin{aligned} \log \Sigma_{L'3-2} = {} & (0.94 \pm 0.05) \log \Sigma_{L'1-0} \\ & - (0.12 \pm 0.02) \log \Sigma_{SFR} \\ & + (1.4 \pm 0.2) \quad \text{(least-squares fitting)} \end{aligned} \tag{14}$$

Downloaded from https://academic.oup.com/pasj/article-abstract/70/3/48/4970741 by Library of Chinese Academy of Sciences user on 02 August 2019

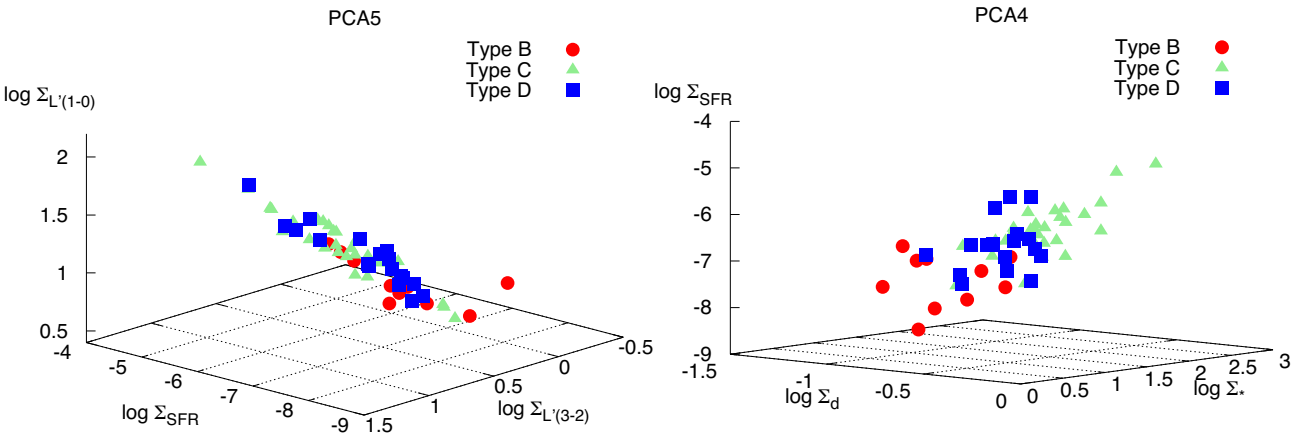


Fig. 3. Plane defined by equation (13) (left-hand panel) and equation (15) (right-hand panel). Figures are oriented so that the best-fitting plane is observed edge-on. Symbols are coded as in figure 1. (Color online)

in the case of surface densities, both with scatter of 0.2 dex (figure 3, left-hand panel). The equations are derived in the same way as in equations (7) and (9) using table 5. The near-constant ratio of the CO intensities, slightly modulated by the *SFR*, is consistent with the results of Onodera et al. (2012), which are that more-massive molecular clouds with higher *SFR* tend to have higher r_{31}. The small but present effect of the *SFR* to CO ratio is visible because the contribution from other parameters (stars and dust) are effectively zero. The local (GMC-scale) SK plots in figure 2 (bottom middle and bottom right) are two-dimensional projections of the plane defined in equation (13).

A number of previous studies have pointed out the possible contribution of stellar surface density to star formation (Blitz & Rosolowsky 2006; Shi et al. 2011; Rahmani et al. 2016; Dib et al. 2017). In this study also, the stellar mass contributes mildly to PC_4 in case of surface densities. The plane formed by $\log \Sigma_{SFR}$, $\log \Sigma_{\rm d}$, and $\log \Sigma_*$ are

$$\log \Sigma_{SFR} = 3.1 \log \Sigma_{\rm d} + 0.67 \log \Sigma_* - 5.5 \quad (\mathrm{PC}'_4 = 0) \tag{15}$$

$$\begin{aligned} \log \Sigma_{SFR} = {} & (2.1 \pm 0.2) \log \Sigma_{\rm d} \\ & + (0.5 \pm 0.2) \log \Sigma_* \\ & - (5.9 \pm 0.4) \quad \text{least-squares fitting} \end{aligned} \tag{16}$$

with a scatter of 0.4 dex (figure 3, right-hand panel). As discussed in subsection 5.1, if dust indeed traces molecular gas better than CO lines on the scales of individual molecular clouds, the relation given in equation (15) can be interpreted as an extended form of the SK relation that connects *SFR* with gaseous and stellar content, valid at GMC scales. The power-law index of the stellar term (0.67 from PCA; 0.5 from least-squares fitting) is roughly consistent with that in recent literature (0.36 in Shi et al. 2011; 0.74 in Rahmani et al. 2016) and theoretical expectations in the case of star formation triggered by two-fluid instabilities (Dib et al. 2017). Blitz and Rosolowsky (2006) show that for pressure-regulated star formation, the stellar contribution has an index of roughly 0.5 and molecular gas density has an index of 2.0 [where equations (15) and (16) indicate that the dust term has an index of 2 to 3]. It should be noted, however, that stellar contribution can be seen only for surface densities [$(-0.26)^2 \sim 6\%$] but is 0% in the case of luminosities. This difference may either indicate that the extended star-formation law is indeed sensitive to density, or simply that the appearance of a stellar contribution is due to small-number statistics in this study.

An interesting feature of equations (13) and (15) is that the relation holds for clouds regardless of evolutionary stage. GMC Types B, C, and D mark evolution timescales of 10 Myr, over which the conversion from gas to stars proceed in tandem with feedback processes from stars, resulting in significant changes in distribution of ISM and stars. Thus, one may expect that clouds of different types would lie on a different relation (provided that any relations exist at this scale). The fact that GMCs of different types spanning $\sim$40 Myr lie on the same planes shown in figure 3 indicate that equations (13) and (15) act as boundary conditions for how physical parameters can change, i.e., can be interpreted as a kind of equation-of-state describing the dynamical equilibrium between the ISM and stellar phases.

5.4 Future work

This paper presents a case study on a late-type galaxy which is relatively metal-poor. There are a number of other physical parameters which are expected to relate to star formation. In particular, metallicity and dynamical parameters

Downloaded from https://academic.oup.com/pasj/article-abstract/70/3/48/4970741 by Library of Chinese Academy of Sciences user on 02 August 2019

(velocity dispersion and larger-scale shear) are not included in the PCA analysis presented here. Further studies should include a significant increase in sample size, spanning a broader range of quantified and catalogued characteristics.

Acknowledgments

The authors thank the referee for helpful comments which improved the paper. S. Komugi is financially supported by the Japan Society for the Promotion of Science (JSPS) KAKENHI (25800114, 15H02074).

References

Blitz, L., & Rosolowsky, E. 2006, ApJ, 650, 933
Bresolin, F. 2011, ApJ, 730, 129
de Vaucouleurs, G. 1959, ApJ, 130, 728
Dib, S., Hony, S., & Blanc, G. 2017, MNRAS, 469, 1521
Dunne, L., Eales, S., Ivison, R., Morgan, H., & Edmunds, M. 2003, Nature, 424, 285
Eldridge, J. J., & Relaño, M. 2011, MNRAS, 411, 235
Ezawa, H., Kawabe, R., Kohno, K., & Yamamoto, S. 2004, Proc. SPIE, 5489, 763
Girardi, L., et al. 2010, ApJ, 724, 1030
Hernández, J., Briceño, C., Calvet, N., Hartmann, L., Muzerolle, J., & Quintero, A. 2006, ApJ, 652, 472
Hollenbach, D. J., & Tielens, A. G. G. M. 1999, Rev. Mod. Phys., 71, 173
Iono, D., et al. 2009, ApJ, 695, 1537
Israel, F. P. 1997, A&A, 328, 471
Jarrett, T. H., Chester, T., Cutri, R., Schneider, S. E., & Huchra, J. P. 2003, AJ, 125, 525
Kawamura, A., et al. 2009, ApJS, 184, 1
Kennicutt, R. C., Jr. 1998, ApJ, 498, 541
Kohno, K. 2005, ASP Conf. Ser., 344, 242
Komugi, S., et al. 2011a, PASJ, 63, 1139
Komugi, S., et al. 2012, ApJ, 757, 138
Komugi, S., Kohno, K., Tosaki, T., Nakanishi, H., Onodera, S., Egusa, F., & Sofue, Y. 2007, PASJ, 59, 55
Komugi, S., Sofue, Y., Nakanishi, H., Onodera, S., & Egusa, F. 2005, PASJ, 57, 733
Komugi, S., Yasui, C., Kobayashi, N., Hatsukade, B., Kohno, K., Sofue, Y., & Kyu, S. 2011b, PASJ, 63, L1
Kuno, N., et al. 2011, in IAU Symp. 277, Tracing the Ancestry of Galaxies, ed. C. Carignan et al. (Cambridge: Cambridge University Press), 67
Leroy, A., Bolatto, A., Stanimirovic, S., Mizuno, N., Israel, F., & Bot, C. 2007, ApJ, 658, 1027
Marigo, P., Girardi, L., Bressan, A., Groenewegen, M. A. T., Silva, L., & Granato, G. L. 2008, A&A, 482, 883
Massey, P., Olsen, K. A. G., Hodge, P. W., Strong, S. B., Jacoby, G. H., Schlingman, W., & Smith, R. C. 2006, AJ, 131, 2478
Miura, R. E., et al. 2012, ApJ, 761, 37
Miura, R. E., et al. 2014, ApJ, 788, 167
Muraoka, K., et al. 2007, PASJ, 59, 43
Muraoka, K., et al. 2016, PASJ, 68, 18
Onodera, S., et al. 2010, ApJ, 722, L127
Onodera, S., et al. 2012, PASJ, 64, 133
Paradis, D., Dobashi, K., Shimoikura, T., Kawamura, A., Onishi, T., Fukui, Y., & Bernard, J.-P. 2012, A&A, 543, A103
Rahmani, S., Lianou, S., & Barmby, P. 2016, MNRAS, 456, 4128
Scoville, N., et al. 2016, ApJ, 820, 83
Shi, Y., Helou, G., Yan, L., Armus, L., Wu, Y., Papovich, C., & Stierwalt, S. 2011, ApJ, 733, 87
Tosaki, T., et al. 2011, PASJ, 63, 1171
Wolfire, M. G., Hollenbach, D., & McKee, C. F. 2010, ApJ, 716, 1191
Wu, J., Evans, N. J., II, Gao, Y., Solomon, P. M., Shirley, Y. L., & Vanden Bout, P. A. 2005, ApJ, 635, L173

Downloaded from https://academic.oup.com/pasj/article-abstract/70/3/48/4970741 by Library of Chinese Academy of Sciences user on 02 August 2019